Fundamental Insight into the Substrate-Dependent Ripening of Monodisperse Clusters

Yves Fukamori,[a] Michael König,[a] Bokwon Yoon,[b] Bo Wang,[a] Friedrich Esch,*[a] Ueli Heiz,[a] and Uzi Landman[b]

Sintering is one of the major routes for the deactivation of surface-supported catalytic particles in heterogeneous catalysis. The two mechanisms that are responsible for such coarsening phenomena are Ostwald ripening, in which larger clusters tend to grow at the expense of smaller ones, and Smoluchowski ripening, in which entire clusters diffuse and coalesce. The sintering properties of cluster-assembled materials can be influenced by tuning the interactions between the particle and the substrate. To explore the fundamental factors that control cluster-ripening mechanisms, we deposited truly monodisperse Pd clusters onto three different model catalysts: bare Rh(111), graphene-Moiré films that were grown on Rh(111) and Ru(0001), and a hexagonal boron-nitride film that was grown on Rh(111). The evolution of particle size and density was tracked by high-resolution scanning tunneling microscopy. The principal microscopic mechanisms that govern the ripening processes on each of these three substrates have been determined from thorough analyses of the cluster heights and size distributions. The ripening mechanisms were related to the distinct cluster-adsorption and atom-detachment energies that were obtained from first-principle calculations. These results elucidate the ripening processes and underlie the formulation of a strategy for optimizing cluster stability against ripening, where both, the binding of the clusters to the surface and that of the individual atoms, must be controlled. Such tuning of the interactions may be achieved through the judicious selection of surfaces with laterally modulated wettability.

Introduction

Heterogeneous catalysis is involved in most of the fundamental processes in modern chemical and petrochemical industries, thus making investigation of catalyst-deactivation processes that lead to the loss of activity and selectivity and decreased lifetime of the catalysts both timely and of utmost importance. In general, one may distinguish four main deactivation mechanisms of heterogeneous catalysts: poisoning, coking, phase transitions, and sintering. The first three processes can be related to complicated chemical changes, whereas sintering, that is, particle coarsening, is commonly driven by thermodynamic processes that operate at elevated temperatures,[1] such as in the steam reforming of methane on oxide-supported Ni particles at temperatures up to 1300 K.[2] The coarsening of catalytically active particles, which often occurs concomitantly with the collapse of support pores/channels at elevated temperatures, results in a dramatic reduction of the active catalytic surface area and a loss of particle-size-specific properties.[3] Consequently, the activity of the catalyst drops.

The main driving force for catalytic sintering is the minimization of the total surface energy of the system. In contrast to most other deactivation mechanisms, sintering is normally irreversible, cannot be cured, and, hence, needs to be prevented from the start. Although the sintering rate can be readily assessed in industrial catalytic systems, rather little is known about the molecular mechanisms, as a result of the complex nature of the catalytic structures, which often consist of metal particles that are loaded in—or supported on—porous oxides. In contrast, model catalysts, such as well-dispersed metal clusters on oxide thin films that are supported on metal/semiconductor single crystals,[4] represent a well-defined chemical environment that can be investigated by using surface-sensitive techniques.

Two main mechanisms have been found to be responsible for cluster sintering: The first one is Ostwald ripening (OR), in which larger clusters grow at the expense of smaller ones. The clusters are supposed to be sufficiently immobile, so that mass transport only occurs through the diffusion of atoms (or small intermediates) that preferentially detach from the smaller clusters. This is a consequence of their higher, curvature-dependent vapor pressure, owing to the Gibbs–Thomson effect. This phenomenon was first described by Ostwald in 1900 for colloidal systems.[5] The second ripening mechanism involves cluster coalescence, also called Smoluchowski ripening (SR). In this mechanism, particle migration and coalescence occur, with

[a] Y. Fukamori, M. König, Dr. B. Wang, Dr. F. Esch, Prof. U. Heiz
Chemistry Department
Technische Universität München
Lichtenbergstraße 4, 85748 Garching (Germany)
Fax: (+49) 89289
E-mail: friedrich.esch@tum.de

[b] Dr. B. Yoon, Prof. U. Landman
School of Physics
Georgia Institute of Technology
Atlanta, Georgia 30332 (USA)

Supporting information for this article is available on the WWW under http://dx.doi.org/10.1002/cctc.201300250.

entire clusters diffusing over the surface and eventually colliding and merging into larger clusters. This mechanism was first described by Smoluchowski in 1916 for coagulation processes in colloids.[6]

Theoretical models have been developed for these above-mentioned ripening mechanisms to describe the profile of the particle-size distribution (PSD), based on an analysis of the particles' dimensions over the entire ripening process.[7] In the case of OR, the kinetics of the process can be described by Lifshitz–Slyozov–Wagner (LSW) theory.[8] This theory was originally derived for precipitation and coalescence in solid solutions, but was adapted by Chakraverty to describe the grain-size distributions in discontinuous thin films.[9] More recently, Finsy further developed this theoretical approach to predict the PSD profile under the following conditions: 1) The particles are fixed in space; 2) they do not interact; 3) the coverage of the diffusing species is constant except for the direct neighborhood of the particles; and 4) transport occurs through diffusion between particles.[10] This PSD only depends on the particle diameter, scaled by the average diameter. The OR process can be limited by either diffusion control, in which diffusion of the atoms is the rate-limiting step, or by interface control, in which the detachment of atoms from the clusters is the rate-limiting step. In either case, the PSD reaches a self-similar shape with a tail in the small-diameter regime, which results from the continuous supply of small clusters. Although smaller clusters form on the surface, initially the total cluster coverage (number of particles) remains constant and the maximum of the PSD does not shift significantly.

For the SR mechanism, Granqvist and Buhrman showed that the PSD corresponds to a log-normal distribution function, which is skewed towards higher particle sizes.[11] Because smaller particles tend to be more mobile, they have a higher probability to sinter and disappear. This consumption of small particles leads to a sharp cutoff of the PSD function at lower particle diameters, an immediate shift of the PSD maximum upon ongoing ripening, and, hence, an immediate decrease in the total cluster coverage. The process of SR can either be limited by migration or by coalescence. By calculating the coalescence time for small Pt clusters assuming that they are spherical and do not wet the substrate, Wynblatt and Gjostein showed that, for particles smaller than 5 nm in diameter, coalescence occurred so fast that migration became the rate-limiting step.[12]

Over the last decade, several experimental studies were performed to investigate ripening processes on real catalysts, as well as on model catalyst systems. Herein, we focus on those studies that attempted to infer which of the two mechanisms was leading to ripening from the PSD. Datye et al. investigated the ripening of technically relevant supported catalysts (e.g., Pd and Pt particles on alumina) by TEM and scanning transmission electron microscopy (STEM).[13] On modulating the experimental conditions so as to select the OR or SR mechanism, the resulting PSD was always characterized by a log-normal distribution function with a tail towards larger particle diameters. The authors concluded that a deduction of the ripening mechanism was not possible based solely on the PSD profile. Simonsen et al. used a planar support of amorphous Al_2O_3 to investi-

gate the ripening of Pt clusters by using TEM.[14] They showed that the ripening of the particles was mediated by OR and that the shape of the PSD sequentially changed during the ripening process from a Gaussian profile to the distribution as predicted by LSW theory, that is, skewed towards smaller particle sizes. In contrast to the work of Datye et al., Simonsen et al. concluded that their experimental conditions, that is, the uniform flat support and the homogeneous initial distribution, were closer to the assumptions made in the LSW model. A more clearly defined model system was adopted by Jak et al. by investigating the growth of small Pd particles on $TiO_2(110)$ by using scanning tunneling microscopy (STM).[7a] The prevailing mechanism for ripening in this system is regarded to be SR for several reasons: The cluster density decreases dramatically with time; the PSD that is obtained at elevated temperatures fits better to a log-normal distribution function; and mobile clusters on the surface are already observed at room temperature. However, another study on this system by Howard et al.[7b] attributed the ripening process to the OR mechanism, thus indicating a critical influence of the initial conditions, such as cluster-size distribution, on the ripening process.

From the above case studies we concluded that the shape of the PSD cannot serve as the only conclusive, discriminating identifier of the ripening mechanism, particularly when starting from an initial broad PSD that convolves with the final PSD resulting from the evolved ripening process.[7a, 13–15] These uncertainties, as well as other factors that complicate the assignment of the ripening mechanism, have been discussed and debated in some detail.[16]

Unlike previous studies, we start here with truly monodisperse Pd clusters that have been size-selected and soft-landed onto highly ordered substrates, thus affording the unique advantage of well-defined initial conditions. Furthermore, we use high-resolution STM as a tool for determining the PSD and, therefore, we can detect the full range of cluster sizes without a lower size boundary, unlike TEM studies, which have limitations in resolving the smallest particles. To the best of our knowledge, the ripening behavior of size-selected clusters, which contain several tens of atoms, has previously been studied experimentally only by the group of Kappes.[17] However, that electron-microscopy study of the ripening of Au clusters on an amorphous carbon surface lacked control over the substrate quality and did not have sufficient lateral resolution to directly distinguish between the OR and SR mechanisms. Furthermore, the diffusion coefficients that were derived in that study seemed to indicate enhanced OR with increasing cluster size. The authors attempted to explain this contradictory finding by suggesting effects that were related to the deposition process and cluster–substrate interactions.

We deposited size-selected Pd clusters onto three well-defined substrates, that is, a bare metallic Rh(111) surface, graphene-Moiré films on Rh(111) and Ru(0001) surfaces, and a hexagonal boron-nitride (h-BN) film that was grown on a Rh(111) surface. These substrates differ in their atom- and cluster-adsorption strengths; the films are (Moiré) superstructures with laterally modulated wettability and comparable long-range order.[18] We investigated the evolution of the rip-
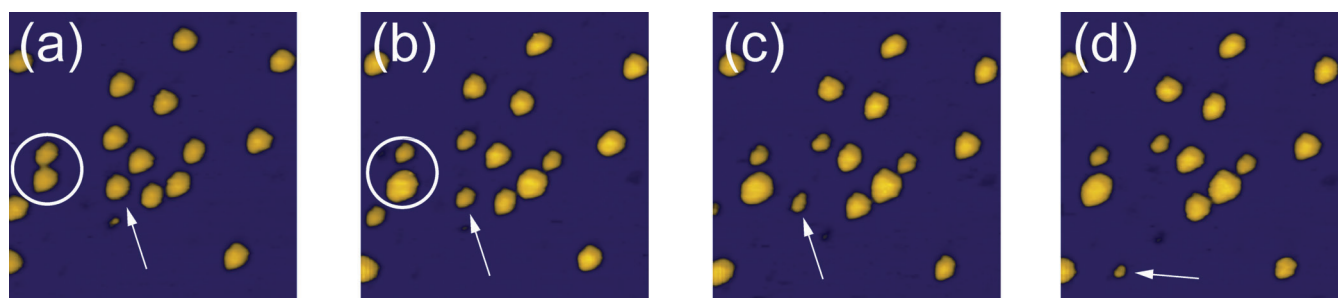
Figure 1. Ripening of Pd_{19} on Rh(111). a) STM image of Pd_{19} immediately after deposition at RT, b) after 7 h 38 min, c) after 17 h, and d) after 17 h 45 min. The clusters coarsened by Ostwald ripening: Some grew larger at the expense of smaller ones (see circles), whose mobility increased dramatically below a certain size (see arrows). Image size: 25×25 nm^2; imaging conditions: $+1.0$ V, 80 pA.

ening processes by annealing to different temperatures to deduce the dominant mechanism in each temperature range. Based on highly resolved STM data from the monodisperse cluster samples, we constructed PSDs from the height histograms. These histograms exhibit peaks that can be assigned to distinct layer heights, unlike, for example, high-quality STEM data, in which, continuous distributions are most often observed (e.g., see Simonsen et al.[14]). The resolution in our experiments allows for studies of a transition between various ripening regimes with unprecedented detail. Our experiments, in conjunction with first-principles density functional theory (DFT) calculations, allow us to gain important insights into the structural and energetic factors that govern the operative atomic-scale mechanisms of mass transport and ripening.

This report is organized as follows: In the next section, we present our results and discuss our findings. We start with a system of Pd clusters that are deposited onto a bare Rh(111) surface, which shows OR processes at room temperature. Next, we investigate Pd clusters that are adsorbed onto a Moiré-patterned g/Rh(111) film, which exhibit ripening according to the SR mechanism for temperatures up to 600 K. Between 600 K and 700 K, a crossover to the OR mechanism is observed. In comparative experiments on the coarsening of Pd clusters on a g/Ru(0001) surface, the SR processes are somewhat damped because of stronger binding to the surface (compared to the g/Rh(111) surface) and the crossover to the OR mechanism occurs at lower temperatures compared to the aforementioned g/Rh(111) case. Lastly, we present results for Pd clusters that are deposited onto a g/h-BN Moiré film, in which the strong interactions between the adsorbed Pd clusters and the substrate completely suppress cluster diffusion and coalescence and coarsening is found to occur through the OR mechanism. We summarize our results in the Conclusion section and give pertinent details about our experimental and computational techniques in the Experimental Section.

Results and Discussion

Pd clusters on Rh(111)

In the first part of this section, we focus on the ripening of metal clusters that are deposited onto a pure metal substrate. Figure 1 shows a series of STM images of Pd_{19} clusters that are

deposited onto Rh(111). Figure 1a shows the topography of the surface after deposition. The Pd_{19} clusters appear as one-layer-high protrusions that all have similar shapes. The relatively low coverage (25×10^{-3} clusters nm^{-2}) was chosen to prevent cluster collisions and merging already on deposition and, hence, to assure the monodispersity of the sample. The observation of a 2D, one-layer-high structure of the adsorbed Pd_{19} clusters on the bare metal surface is supported by our first-principles calculations. Indeed, these calculations have shown (Figure 2) that the optimal geometry of the adsorbed cluster on the Rh(111) surface is 2D (Figure 2a), with the 3D, two-layer isomer (Figure 2b) having a significantly higher energy (5.95 eV).

The STM images in Figure 1b–d show the effects of the ripening process over several hours under ultrahigh vacuum (UHV) conditions at room temperature. The measurements were stable enough to observe the same area over a period of 12 h. About 7 h after the deposition, some Pd clusters had grown in size, whereas others had become smaller. The most prominent example of one cluster shrinking and another growing in size are the two adjacent clusters marked by a circle in Figure 1a,b. Whereas the large Pd clusters stay immobile during the ripening process, the shrinking cluster (marked by an arrow) moves from its position after 17 h and starts to diffuse over the surface. The time interval between Figure 1c and Figure 1d is only 45 min, thus showing a dramatic increase in the cluster mobility.

From the time series in Figure 1, we conclude that OR already occurs at room temperature, because we can clearly observe couples of adjacent Pd clusters in which one cluster grows at the expense of the other. The fact that we only observe one-layer-high clusters results from the strong metallic binding of the Pd cluster atoms onto the Rh(111) substrate. Notably, this strong binding does not prevent the ripening process: At the periphery of the 2D cluster, single Pd atoms may detach from the cluster with a relatively small energy cost of about 0.8 eV (Figure 3a,b). These observations are in accord with the investigations of similar metal-supported metal-cluster systems.[19] This 2D detachment (evaporation) of the material leads to the almost-complete dissolution of some clusters, such as the cluster indicated by an arrow in Figure 1. As soon as the shrinking clusters reach sizes of roughly five atoms, they become much more mobile. This mobility indicates that it is
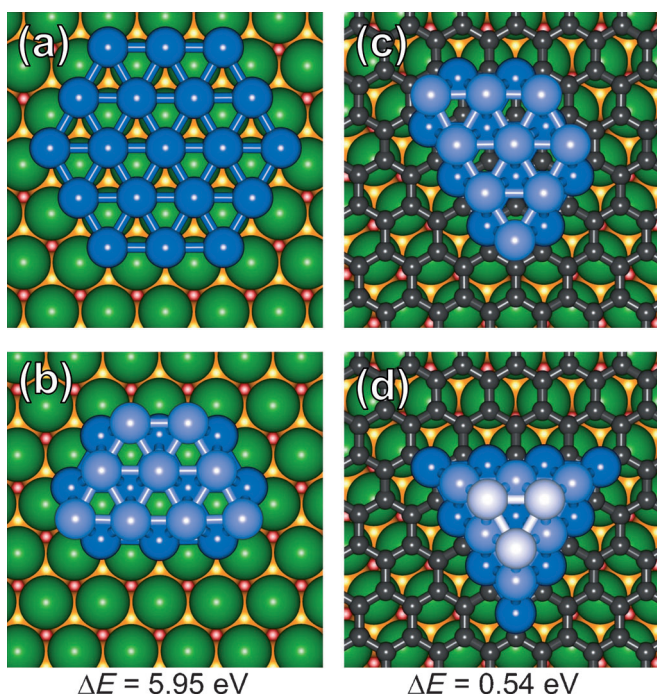
$\Delta E = 5.95$ eV $\Delta E = 0.54$ eV

Figure 2. Optimized atomic configurations that were obtained from first-principles DFT calculations for Pd_{19} clusters on bare Rh(111) (a, b) and on g/Rh(111) (c, d). On Rh(111), the most-stable configuration is the 2D (one-layer) configuration (a), whereas the 3D (two-layer) configuration is 5.95 eV higher in energy (b). On the r-hcp sites of g/Rh(111), 3D structures are preferred, with a most-stable configuration of 2 layers (c), whereas the three-layer configuration is only 0.54 eV higher in energy (d). Rh substrate atoms are depicted by large green (first layer), orange (second layer), and red spheres (third layer). Carbon atoms of the graphene-Moiré film are depicted as small dark-gray spheres (c, d). Pd cluster atoms in direct contact with the underlying surface are depicted as dark-blue, light-blue (second cluster layer, b–d), and whitish-blue spheres (third cluster layer, d).

not the diffusion, but the detachment process of the transporting species that limits the OR. Our findings are supported by other examples of homogeneous and heterogeneous metal-on-metal studies, which predict a decrease in the binding energy of clusters once they contain fewer than six atoms;[20] consequently, the mobility of the cluster increases.

In Figure 4, which was recorded at a slightly increased temperature of 308 K, in three consecutive STM topographs, taken at 6 min intervals, we observe a shape transition of the larger cluster into a quasi-hexagonal shape, whereas the smaller cluster in the lower part of the image reversibly changes from a triangular into a truncated triangular shape and back again. By deconvolving the shape of the STM tip from the cluster topography, we can estimate that the Pd cluster consists of about 15 atoms, which are arranged in a triangular manner, as indicated by a comparison between the cluster profile and a ball model of Pd_{15} in Figure 4a (see the triangular 2D cluster, bottom right). Compared to the initially deposited Pd_{19} clusters, the triangular Pd cluster decreased in size, whereas the quasi-hexagonal cluster took up atoms (through detachment from smaller clusters) and became considerably larger than Pd_{19}. The shape changes during the ripening of 2D clusters as observed in Figure 4 are facilitated by the weaker Pd–Pd bind-
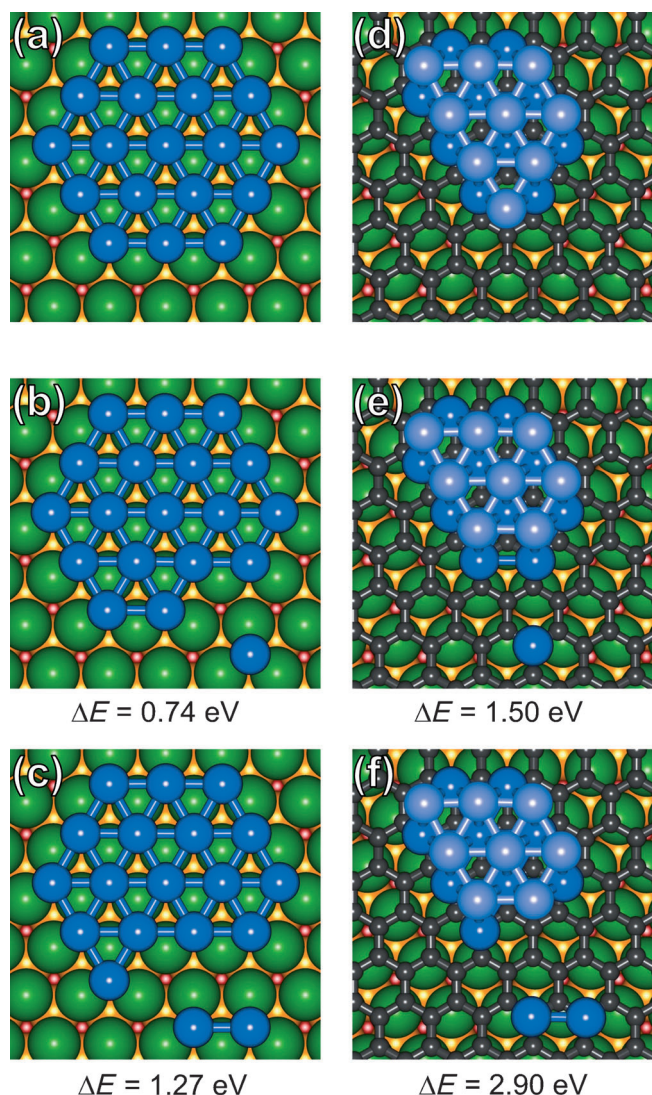

$\Delta E = 0.74$ eV $\Delta E = 1.50$ eV

$\Delta E = 1.27$ eV $\Delta E = 2.90$ eV

Figure 3. Optimized atomic configurations that were obtained from first-principles DFT calculations for Pd_{19} clusters on bare Rh(111) (a–c) and on g/Rh(111) (d–f). Starting from the most-stable configurations (a, d), we show the atomic configurations that correspond to the lowest-energy single atom (b, e) and their related dimer-detachment processes (c, f). The single-atom-detachment process on Rh(111) entails a transition-state barrier of 0.89 eV, which is encountered 0.6 Å prior to reaching the local-energy minimum shown in (b); overall the atom covers in this detachment process a distance of 2.55 Å with respect to the initial configuration, and the final configuration is 0.74 eV higher in energy. The corresponding detachment of a Pd dimer entails a total energy increase of 1.27 eV (c). In contrast, the single-atom-detachment process on g/Rh(111) leads to an atom displacement of 2.63 Å prior to reaching the local-energy minimum shown in (e); the final configuration is 1.50 eV higher in energy, which is twice the value for single-atom detachment from the cluster that is adsorbed on the bare Rh(111) surface. The detachment of a Pd dimer from the Pd_{19} cluster on g/Rh(111) even entails an overall energy increase of 2.90 eV (f). For the color legend, see Figure 2.

ing at the cluster periphery compared to the stronger binding of the cluster to the substrate. A hexagonal (111) surface of a fcc crystal, such as Rh, can expose two kinds of steps, A and B, which differ in their direction with respect to the underlying layer. Thus, the triangular islands can be oriented in two ways, which differ by an angle of 60°. The assignment of a particular
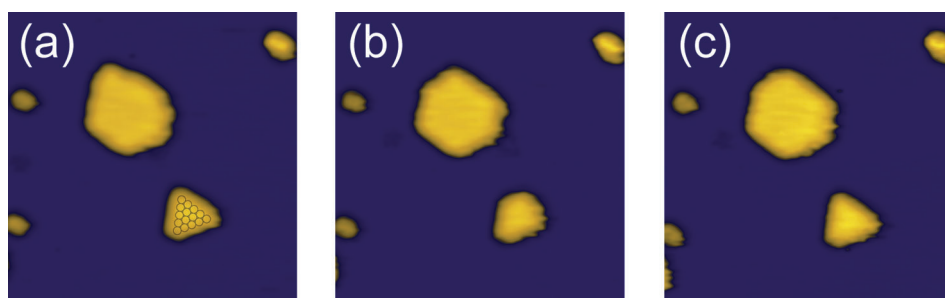
Figure 4. Cluster-shape fluctuations of Pd clusters on a Rh(111) surface during the ripening process at 308 K. The cluster below changes from a triangular shape (a) into a truncated triangular shape (b) and back into a triangular shape (c). As a guide to the eye and considering the tip-convolution effect, an atomic model of that cluster has been added to (a). Image size: 10×10 nm^2; imaging conditions: -1.0 V, 100 pA; time step between consecutive images: 6 min.

step type can be achieved by comparing the single-crystal directions of the Rh substrate with the registry of a superstructure, such as the graphene-Moiré film discussed in the next section. This result leads us to conclude that the triangular cluster in the lower part of Figure 4 is delimited by A steps. This shape appears immediately after deposition. The presence of triangular islands, which are confined by A steps and in concomitance to hexagonal islands, is similar to the findings for atomically deposited metal-on-metal systems within the same temperature range, in which kinetic limitations have been postulated and the preference for A steps has been explained by the slower diffusion of atoms along the B steps.[21] The same kinetic limitations might apply in our case.

From these above result, we conclude that, for Pd clusters on a Rh(111) surface, the ripening of monodisperse clusters proceeds at room temperature by OR, thereby exhibiting pronounced shape fluctuations during the process.

Pd clusters on graphene/Rh(111)

Next, we will focus on Pd$_{19}$ clusters that are deposited onto a g/Rh(111) surface, that is, a graphene-Moiré film that is supported on Rh(111). The g/Rh(111) film was formed by the catalytic dehydrogenation of ethylene adsorbed onto the Rh(111) surface at high temperatures (see the Methods section). Owing to the mismatch between the lattice constants of graphene and Rh(111), a Moiré superstructure comprised of (12×12) carbon unit cells on (11×11) Rh unit cells, with an approximate periodicity of 3.0 nm, is observed. The topographic and electronic structure of such a graphene-Moiré structure has previously been investigated both experimentally and theoretically.[22] In the STM images, the surface appears with a corrugation of up to 0.6 Å. The maxima correspond to positions at which the graphene rings are centered on top of a substrate atom (r-top) and the minima to positions that are centered on hollow sites (r-fcc and r-hcp), at which the graphene interacts more strongly with the metal substrate. The latter areas are prone to cluster adsorption, whereas, at the former locations, the interactions with the metal clusters are relatively weak.[18b, 23] This spatial variability of the interactions between the cluster and the underlying graphene surface gives rise to a superstructure

with laterally modulated wettability. For the assignment of the high-symmetry locations in a structural model, see, for example, Wang et al.[22]

Figure 5a shows an STM image of a g/Rh(111) sample that was dosed with Pd$_{19}$ clusters at RT under soft-landing conditions. In the STM image that was taken at 300 K, we observe a perfectly grown graphene-Moiré film that is decorated with Pd$_{19}$ clusters. The cluster coverage is 18×10^{-3} clusters nm^{-2} (about 7% with respect to the number of Moiré supercells). From the image in Figure 5a, it is apparent that two different cluster heights mainly occur and that the higher clusters appear wider, owing to a larger tip-convolution effect. Because tip convolution does not affect the height determination as obtained from the STM topography, cluster heights can be reliably measured with a precision of down to about 0.1 Å. Extensive height statistics have been accumulated for at least 80 clusters per sample; the resulting height histograms, normalized to relative frequencies, are shown in Figure 5b and serve as the PSD of the clusters that are present on the surface. The noticeable bimodal cluster-height distribution in the image at 300 K (Figure 5a) is distinctly mapped in the corresponding histogram. The two cluster heights are attributed to two types of isomers of Pd$_{19}$ that are two- and three layers high (similar to the case for g/Ru(0001)[18b]). The layer distance of 2.5 Å, as marked in the histograms by dashed lines, is comparable to the diameter of Pd in the bulk, but larger than the step height on a Pd(111) surface. The peaks in the histogram indicate that the clusters have a layered structure, which already starts at small sizes. In any case, the smaller two- to three-layer-high clusters also show intermediate intensity between the two neighboring peaks in the histogram, which may indicate that there are more than just two isomers that show different electronic coupling to the substrate. However, these differences are of diminishing influence for larger clusters. Upon closer examination of the STM image, we observe that the Pd$_{19}$ clusters are exclusively bound to ring-hollow sites of the Moiré superlattice, with roughly equal probabilities in r-hcp and r-fcc.

These above observations are supported by our calculations on two- and three-layer Pd$_{19}$ clusters that are adsorbed onto g/Rh(111) at r-hcp sites (Figure 2c,d). These two 3D surface-supported isomers are predicted to be separated by a relatively small energy (0.54 eV). We summarize these findings by concluding that, on the supported graphene film, the Pd$_{19}$ clusters do not completely wet the surface but tend to retain a 3D structure as a consequence of the stronger binding within the cluster compared to the cluster interactions with the substrate; this effect has been discussed previously for adsorbed Pd$_{19}$ and Pd$_{20}$ onto g/Ru(0001).[18b] The experimental observations
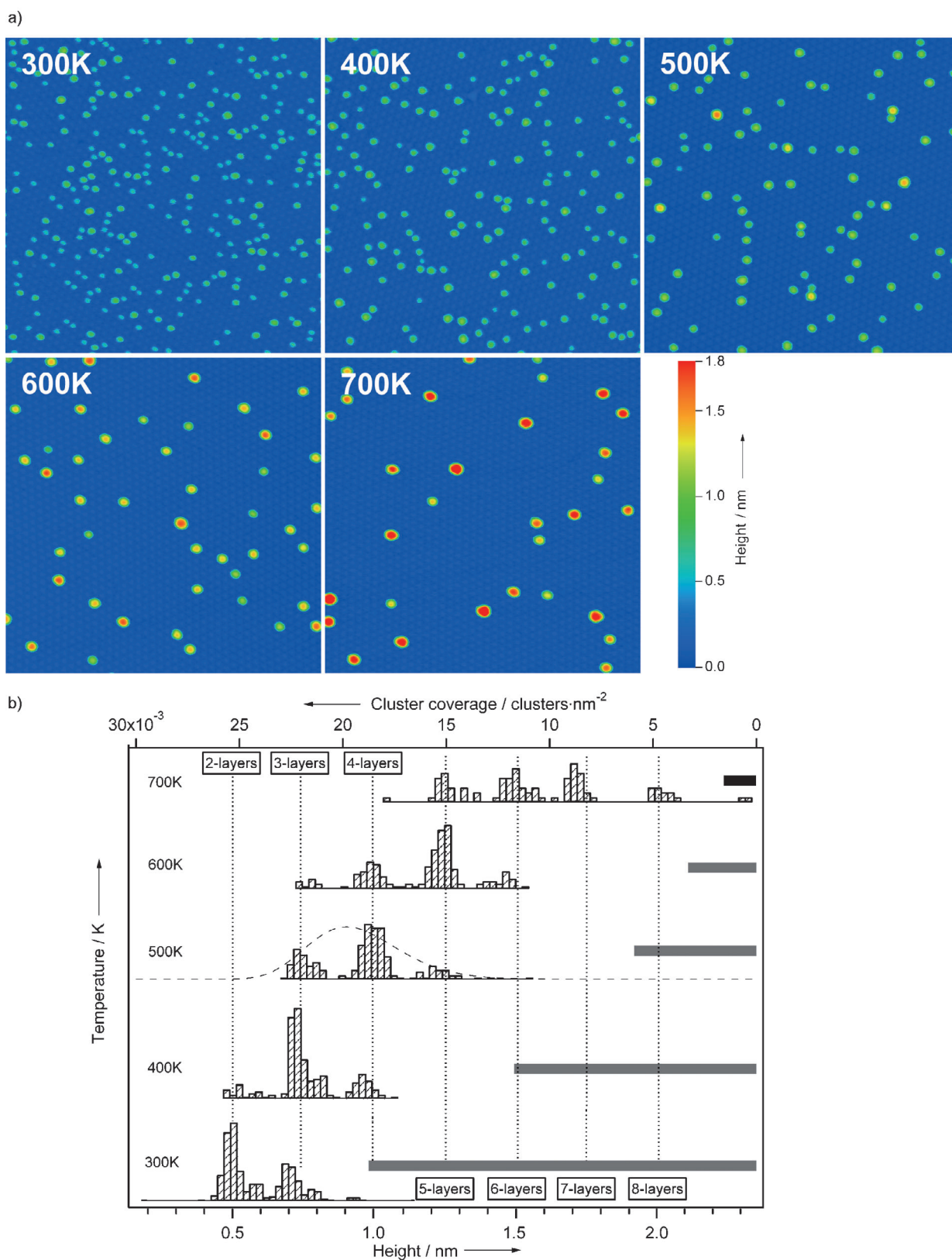
a)

b)

Figure 5. a) Ripening of Pd_{19} clusters on a g/Rh(111) surface upon sample annealing for 5 min at the indicated temperature; the images were recorded at RT. Image size: 120×120 nm²; imaging conditions: +0.5 V, 1 pA. b) Bottom axis: Particle-size distributions that correspond to the images in (a). The PSDs are obtained as height histograms, normalized to the relative frequencies; the analyzed surface areas are larger than the shown cutouts and correspond to 120×180 nm² (300 K and 400 K), 160×240 nm² (500 K), and 200×300 nm² (600 K and 700 K). Distinct layer peaks are resolved. As a guide to the eye, the 500 K data are fitted to the log-normal function of Granqvist and Buhrman.[11a] Top axis: Observed cluster coverage at each annealing temperature, as represented by gray bars. The shift in PSDs to larger cluster size, their sharp lower-edge cutoff, and the loss in cluster coverage indicate that an SR mechanism is dominant for annealing temperatures of up to 600 K; thereafter OR takes over.

of two- and three-layer clusters are in agreement with the small energy difference from the calculations. For further DFT results, see the Supporting Information.

Upon successive annealing for 5 min at increasingly higher temperatures in steps of 100 K and subsequent measurements by STM at room temperature, we observe a growth in the cluster height in the STM images, accompanied by a decrease in the cluster number (Figure 5 a). Notably, the images in the sequence are all of the same size and are representative cutouts taken from (at least) six-fold-larger images. After the final annealing at 700 K, only a few very large clusters remain on the graphene surface. The whole process, as shown in the histograms in Figure 5 b, is manifested by a continuous shift in the PSD maxima and by a lower onset to larger cluster heights. Moreover, the cluster coverage, depicted as horizontal bars, also diminishes dramatically with each annealing step: At 400 K, two thirds of the initial coverage has already disappeared and the corresponding PSD shows a clear decrease in the two-layer clusters; the three-layer clusters start to dominate and the first four-layer clusters appear. This shift to larger sizes continues at higher annealing temperatures, with the PSD remaining similar in shape at 500 K, slightly broadening at 600 K, and strongly broadened at 700 K. Throughout this process, the cluster coverage continues to drop considerably until only roughly one tenth of the initial cluster coverage is left.

From these observations, it is clear that the surface has undergone a ripening process. The continuous shift in the maximum height distribution to higher values, the sharp distribution cutoff at low values, and the tail at high cluster heights, as well as the immediate change in cluster coverage upon annealing, unequivocally point to an SR mechanism. The corresponding log-normal distribution curve[11a] has been tentatively fitted to the PSD after annealing at 500 K and clearly indicates a high-particle-size tail. Further support for the suppression of the OR process and the emergence of SR as the dominant ripening mechanism on this graphene film comes from our first-principles calculations; indeed, for the two-layer Pd_{19} cluster that is adsorbed at the r-hcp site on g/Rh(111), these calculations predict relatively high monomer- and dimer-detachment energies (1.5 eV and 2.9 eV, respectively, see Figure 3 e, f). These high detachment energies inhibit the onset of OR, at least up to relatively high temperatures (see the following discussion).

The cluster distribution only broadens significantly after annealing to 700 K, which indicates an onset of the OR mechanism between 600 K and this temperature. However, small clusters could not be observed after annealing, possibly owing to the high mobility of the smaller clusters at elevated temperatures, thus leading to their disappearance before the sample has cooled to room temperature. At these moderate maximum annealing temperatures, desorption of Pd atoms is unlikely to occur.

The SR mechanism implies the subsequent formation of increasingly large clusters, with increasing adhesion to the surface and, hence, decreasing diffusion propensity. Whether this increasing adhesion is limited to a critical footprint size or not is the topic of ongoing investigation in our laboratories.

The above observation of the onset of an SR process much prior to the OR mechanism is rather unique. One can estimate the stability of particle-assembled catalysts on weakly interacting supports based on the empirical Hüttig temperature, which states that atoms detach from kinks and edges at a temperature of about 30 % of the melting temperature,[24] and, consequently, OR can be expected from this temperature on. Based on this rule-of-thumb, one may expect OR to set in for Pd particles at about 550 K, which is close to that found in our measurements.

To disentangle the contributions from SR and OR by a mild suppression of the SR process, the cluster-adsorption energies have to be increased. For this purpose, we studied the ripening on g/Ru(0001), which showed a Moiré structure of similar periodicity and corrugation to that found on the g/Rh(111) surface, but was characterized by a somewhat stronger interaction with deposited Pd clusters (the binding energy of Pd_{19} was calculated to be about 0.6 eV higher on g/Ru(0001), see below). Owing to the higher activation energy that is needed for cluster migration on the g/Ru(0001) surface, the SR on this surface is dampened compared to that on g/Rh(111) at comparable annealing temperatures. Thus, at 500 K, the PSD of Pd clusters on the g/Ru(0001) surface peaks at three layers, whereas, on the g/Rh(111) surface, clusters of up to five layers are already formed at that temperature. At 600 K, a broadening of the PSD characteristic for the OR mechanism is clearly observed on g/Ru(0001); that is, at a temperature that is about 100 K lower than on g/Rh(111) (see the Supporting Information, Figure S1). In addition, clusters of smaller heights are observed in the broadened PSD and the cluster coverage remains unchanged during annealing at 500 K and 600 K, whereas it only decreases again after annealing to 700 K, once the smaller clusters have disappeared.

We conclude that the higher binding energies of the Pd clusters to the g/Ru(0001) surface underlie a suppression of the SR mechanism, so as to maintain a population of smaller clusters at corresponding applied annealing temperatures. Because smaller clusters have a higher vapor pressure, owing to the Gibbs–Thomson effect, OR is observed at a lower annealing temperature than the aforementioned g/Rh(111).

The stronger binding of the Pd clusters to g/Ru(0001) compared to g/Rh(111) could be substantiated by the calculations: The adsorption energies of the Pd_{19} cluster for the two systems are 6.12 and 5.51 eV, respectively, that is, the cluster binding to the g/Ru(0001) surface is stronger by 0.61 eV. These energies are calculated according to: $[E(g/M)+E(Pd_{19})]-E(Pd_{19}/g/M)$, in which $E(x)$ is the total energy of the indicated system and M is either Ru(0001) or Rh(111). Notably, $E(Pd_{19})$ is the total energy of the isolated Pd_{19} cluster in the corresponding optimized adsorbed configuration.

Upon the onset of OR, one would expect to observe a relative abundance of very small clusters that result from shrinking (owing to atom detachments). On the g/Ru(0001) substrate, this formation of small clusters occurred rarely and on the g/Rh(111) it was impossible to observe. Although small clusters may have formed on the g/Rh(111) surface, the dominance of small-cluster diffusion at high temperatures prohibits in situ

measurements; on studying the samples with STM at room temperature after the annealing stage, aggregation had already taken place.

The cluster–surface interactions can be increased even further by switching to an isovalent substrate, hexagonal boron-nitride, in which the two carbon atoms of the graphene unit cell are replaced by boron and nitrogen.

Pd clusters on h-BN/Rh(111)

A hexagonal boron-nitride film was prepared by the catalytic dehydrogenation of borazine at high temperatures on Rh(111). This process leads to the formation of a Moiré superstructure with a periodicity of about 3.2 nm, which corresponds to a coincidence lattice of (13×13) h-BN units on (12×12) Rh unit cells.[25] This superstructure appears as a one-layer mesh with pores of widths of about 2 nm, which host the deposited clusters and are known from literature reports to be good trapping centers for molecules and clusters.[18a, 26]

To gain further insight into the mechanisms of cluster ripening on this substrate, a h-BN/Rh(111) sample that was dosed with Pd_{19} clusters was investigated by STM at room temperature and after annealing at 500 K and 700 K. Similar to Figure 5 a, b, Figure 6 shows three STM images and their corresponding height histograms. The initial coverage of the clusters was 8.5×10^{-3} clusters nm^{-2} (about 4% with respect to the number of Moiré supercells); the sample was cooled to room temperature before scanning.

From the STM images in Figure 6, we observe that, over the temperature range of our study, the clusters on h-BN/Rh(111) do not grow in height as notably as on the graphene substrates (see above). However, in contrast to the graphene substrates, a considerable amount of very small particles appear at 700 K. A closer examination of the STM images reveals that the clusters are located inside the pores and are mostly adsorbed at their rim. On analyzing the corresponding height histograms (Figure 6, right), the maxima of the PSDs do not shift to larger cluster heights; whereas the PSD does not change much upon annealing at 500 K, it broadens at 700 K and small one-layer-high clusters are ob-

served in both, the histogram and in the corresponding STM image. The different layers do not appear well-separated in the histogram as for the g/Rh(111)-supported cluster sample (Figure 5 b), because the h-BN film is not as uniform and regular as the graphene films and because the binding and electronic interactions with the substrate are stronger (see discussion by Dil et al.[26]). The PSD maximum is always about three layers, but two- and four-layer clusters are also already present at 300 K. In both the STM images and histograms, the coverage remains essentially constant over the whole temperature range, within the limits of precision of our coverage determination; thus, the Pd clusters are much more stable on h-BN/Rh(111) than on the graphene superstructures.

This result indicates that the binding of the Pd clusters to the h-BN/Rh(111) substrate is sufficiently strong as to essentially suppress SR. The broadening of the PSD at 700 K, as well as the constant cluster coverage, are strong indications of OR. The histogram that is obtained after annealing to 700 K can be tentatively fitted to the distribution profile proposed by Finsy[10] and shows a tail towards low particle diameters, as predicted for the OR mechanism. The increased presence of
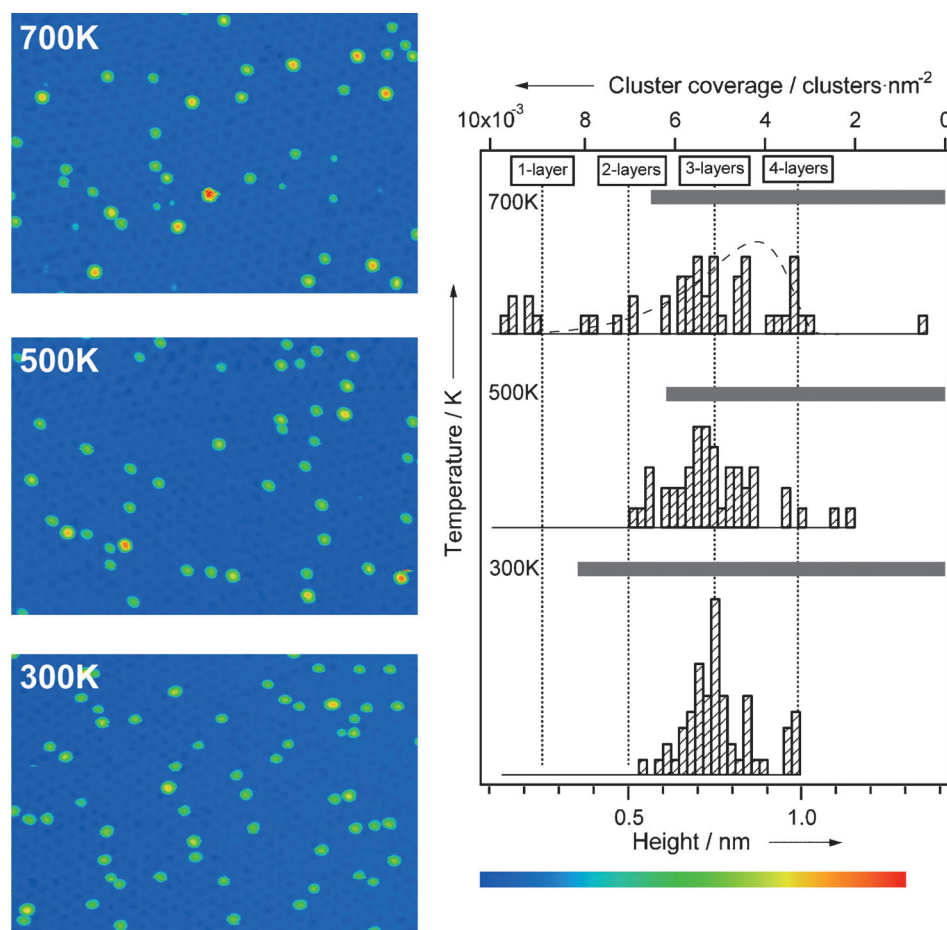

Figure 6. Left: Ripening of Pd_{19} clusters on a h-BN/Rh(111) surface upon sample annealing for 5 min at the indicated temperature. Image size: 75×100 nm²; imaging conditions: +1.0 V, 1 pA. Right: Bottom axis: Particle-size distributions that correspond to the images on the left. The PSDs are obtained as height histograms, normalized to the relative frequencies. As a guide to the eye, the 700 K data are fitted to the model of Finsy.[10] Top axis: Observed cluster coverage at each annealing temperature, as represented by gray bars. The cluster coverage does not decrease as much as for the graphene-Moiré samples. The broadening of the PSDs, without a shift, and the almost-constant cluster coverage indicate an OR mechanism.

small particles might also be partly related to a footprint-related trapping at defect sites; for this reason, clusters of this type were not included in the fit.

Discussion

In this study, we explored two ripening mechanisms of size-selected Pd clusters that were adsorbed onto solid surfaces: Ostwald and Smoluchowski ripening. With atoms taken as the mass-transport agents in the OR mechanism, two possible rate-limiting processes may be considered: 1) Interface control, in which the rate-limiting step involves the detachments of atoms from the smaller clusters, and 2) diffusion control, in which the rate is governed by the surface diffusion of the atoms. Because the barriers for atom diffusion are relatively low on the metal surface,[20b, 27] as well as on the epitaxial graphene surface (both local, single-step site-to-site hopping barriers, and global diffusion barriers from one Moiré cell to the next),[18b] we conclude that the detachment of atoms from the clusters is the operative rate-limiting process in the OR mechanism.

For the OR mechanism to dominate over SR, the following conditions have to be fulfilled: First, the binding of the clusters to the substrate has to be sufficiently strong to anchor them at their adsorption sites. Here, this condition is fulfilled for the metal-on-metal system, based on the observation that the gas-phase 3D clusters transform into 2D islands and "wet" the metal substrate upon deposition and adsorption (Figure 1 and Figure 2 a, b). On h-BN/Rh(111), the binding of the clusters to the substrate is enhanced by the additional trapping potential at the rims of the pores.[26a] Second, the atom-detachment energy of the cluster has to be low enough so that atoms can leave the cluster. The relatively low energy value of about 0.8 eV, as obtained from our first-principles calculations for atom detachment from the interfacial periphery of the adsorbed 2D Pd_{19} island on bare Rh(111), is consistent with this requirement; notably, our calculations indicate an energetically unfavorable dimer detachment. The atom-detachment energy is determined by the local coordination environment of the detaching atom and, consequently, its value is essentially independent of cluster size, except for very small clusters, for which incomplete coordination lowers the detachment energy. However, notably, the diffusion of adsorbed clusters also becomes energetically more favorable at small cluster sizes. Therefore, for circumstances that involve small enough clusters and higher temperatures, competing coarsening mechanisms (that is, the aforementioned OR and SR modes) may operate, with one of them eventually dominating.

In cases in which the SR mechanism dominates at low temperatures, OR processes may only occur if the cluster-diffusion barriers increase strongly with size (thus quenching the SR process). Under such circumstances, a critical cluster size may be reached during the SR process, at which the detachment of single atoms is energetically favored over diffusional displacement of the entire cluster. If this process occurs, the OR mechanism takes over, accompanied by an increased concentration of transporting species on the surface, which is the case for Pd clusters on g/Rh(111) and g/Ru(0001). Because Pd clusters adsorb onto the g/Ru(0001) surface with a higher binding energy than on the g/Rh(111) one, the SR mechanism is partially suppressed on the former surface at lower temperatures. This result is confirmed by the observed PSD broadening after annealing at 600 K for g/Ru(0001) and at 700 K for g/Rh(111).

Cluster-ripening processes can be strongly influenced by the presence of adsorbates. Indeed, the induction of cluster diffusion and the coalescence (i.e., the SR mechanism) of small Pt clusters on a g/Ir(111) surface by CO adsorption have recently been reported.[28] In this system, the graphene film is characterized by a rather weak interaction with the underlying Ir(111) surface and the Moiré superstructure forms through pinning by the adsorbed clusters. Unpinning of the clusters (caused by CO adsorption) induces the diffusion and coalescence of clusters of less than 10 atoms, although its precise mechanism is not yet understood. Because g/Rh(111) and g/Ru(0001) are stable superstructures that are characterized by much stronger interactions between the graphene layer and the metal surface (compared to that operating in the case of g/Ir(111)) and because CO desorbs at annealing temperatures above 400 K,[29] we do not expect the onset of such an adsorbate-induced SR mechanism in our systems. Adsorbates may also influence the atom-detachment energies, thus favoring the OR mechanism. Such effects have been demonstrated by Di Vece et al. in an X-ray diffraction study on Pd nanocluster films in the presence of hydrogen (1 bar) at room temperature.[30] The sublimation energy of Pd decreases with increasing hydrogen concentration and is about 50% lower at a H/Pd ratio of 0.3:1.[31] However, we exclude such an effect in our study under UHV conditions.

In light of our findings, a strategy for the reduction of cluster ripening can be formulated. Graphene-Moiré is a most favorable support for the suppression of the OR mechanism of cluster coarsening because of its laterally modulated wettability, that is, transition-metal clusters bind on the Moiré-patterned surface at locations that are characterized by relatively higher adsorption energies (wettable zones of the surface), with the inhibition of detachment and transport of atoms (serving as the mass-transporting agents) from the clusters, because these processes require transit into areas of the Moiré pattern that are characterized by a significantly weaker adsorption interaction. Consequently, on graphene-Moiré surfaces, cluster stability towards ripening is largely determined by the cluster-adsorption energies. Because these adsorption energies may be relatively small, the onset of cluster diffusion (that is the SR coarsening mechanism) may already occur at relatively low temperatures (e.g., 400 K). In contrast, on the bare metal substrate, the cluster-adsorption energies, as well as the adsorption energies of individual atoms, are high, which facilitates atom detachment and diffusion and decreases the thermal stability of the cluster, this time through the OR mechanism. An intermediate case is represented by the h-BN/Rh(111) substrate, in which the laterally modulated wettability of the Moiré superstructure is accompanied by a higher cluster-adsorption energy. This combination results in increased cluster stability (up to temperatures of at least 500 K) on this surface.

We conclude that the significant success of oxides as stabilizing agents for the support of catalytically active species is related to a similar principle of laterally modulated wettability: Whereas defects act as randomly distributed binding sites (wettable zones), stoichiometric areas in between, in which the binding to the surface vanishes, block the transport of OR diffusing species. This result leads us to suggest that periodic wettability control may be a fruitful concept for the rational design of new catalysts with enhanced stability against sintering.

Conclusions

In this paper, we have reported on the ripening of size-selected and soft-landed Pd clusters on three different substrates: a bare metallic Rh(111) surface, graphene-Moiré films on Rh(111) and Ru(0001) surfaces, and a hexagonal boron-nitride-Moiré film on a Rh(111) surface. These substrates differ in their long-range order, as well as in their atom- and cluster-adsorption strengths. By using STM, we observed different ripening behaviors on these substrates and determined their particle-size distributions through a thorough analysis of the observed cluster heights after each annealing step. The initially monodisperse cluster distribution allows for an unambiguous assignment of the ripening mechanisms, based on the resulting particle-size distributions: On the bare metal surface and on h-BN/Rh(111), the Pd clusters grow exclusively by Ostwald ripening, owing to the stronger binding of the cluster to the substrate. In contrast, on epitaxial graphene, the clusters ripen by Smoluchowski ripening up to 600 K and only then a crossover to Ostwald ripening sets in.

Based on first-principles DFT calculations, we have also gained important insights into the structural and energetic factors that govern the operative atomic-scale mass-transport and ripening mechanisms. These calculations explored the nature and strength of the bonding of the cluster to the surfaces, their dependence on the supporting surface, and the structure of the adsorbed cluster, as well as the energies of atom and dimer detachment from adsorbed clusters. The combined experimental and theoretical investigations allowed us to relate the differences between the ripening behaviors to distinct properties of the different substrates. These results suggest a strategy for optimizing the stability of surface-supported clusters against ripening. Accordingly, we conclude that in attempts to control particle coarsening on a surface one must optimize both the binding of the entire adsorbed clusters to the substrate—which plays a key role in cluster-migration/coalescence processes, termed Smoluchowski-ripening—and the interactions of single atoms or very small clusters, which serve as mass-transport species in the Ostwald-ripening. Such circumstances may be realized by the judicious choice of surfaces with laterally modulated wettability. On such surfaces, the stronger binding of adsorbed metal clusters at particular sites (wettable zones) anchors them to these locations and the relatively weak interactions of single metal atoms with non-wettable regions of the substrate causes their preferential residence in the wettable zones (which act as effective catchment

basins). Our study shows that surfaces with modulated wettability, that is, graphene-Moiré and hexagonal boron-nitride-Moiré films that were grown on metal surfaces, could be useful as model systems for the control of the coarsening of adsorbed particles. The information that was gained in this investigation provides the impetus for the further development of stable effective nanocatalytic systems and investigations of their stability and catalytic properties through the use of surface-supported size-selected clusters.[32]

Experimental Section

Methods

The production of size-selected Pd clusters by a high-frequency laser-evaporation cluster source has been reported elsewhere.[33] The kinetic energy of the impinging clusters was controlled to be low enough (mean kinetic energy: 3 eV) so that non-destructive, soft-landing conditions were fulfilled. The clusters were deposited at RT. The Rh(111) crystal was cleaned by repeated cycles of Ar$^+$ sputtering and consecutive annealing at 1223 K. The graphene monolayer on a Rh(111) surface was prepared by exposing the sample to ethylene (6×10^{-7} mbar) for 3 min at 1123 K. This procedure led to a well-ordered Moiré structure that has been extensively described in the literature.[22,34] Accordingly, the h-BN-Moiré structure on Rh(111) was prepared by exposing the crystal to borazine (6×10^{-7} mbar) for 3 min at 1108 K. Structural and theoretical investigations on this nanomesh can be found in the literature.[25b,35]

All of the STM images of the clusters were recorded with extremely low scan velocities in the order of $\leq 100\ \mathrm{nm\,s^{-1}}$, low bias magnitudes of ≤ 1 V, and low tunneling currents to minimize the interactions with the tip. On the graphene substrates, particularly low tunneling currents of 1 pA had to be chosen (Omicron VT-STM). The low scan velocities require extreme imaging stability: To investigate large areas with statistical relevance, as in Figure 5 and Figure 6, the imaging conditions have to remain stable for several hours. Tip-convolution effects lead to apparent lateral dimensions that are much larger than the "real" ones, whereas the cluster-height determination (topographic maxima) is accurate, with an overall precision down to 0.1 Å. Therefore, the indicated histograms are based on the cluster-height analysis, in contrast to the diameter or area as usually indicated in TEM studies. The histograms are gained from large-scale images ($\geq 15\,000$ nm^2), in which several hundreds of clusters are initially present and sufficiently dilute cluster concentrations are maintained ($\times10^{12}$–$\times10^{13}$ cm^{-2}). The vertical scale was calibrated to the step height of Rh(111), 2.20 Å, respectively of Ru(0001), 2.15 Å.

The images were corrected by subtracting a plane and by aligning the median values of adjacent horizontal rows. After automatic particle detection based on a fixed threshold, the height distributions of the clusters were determined in two different ways: 1) The g/Rh(111) sample showed a rather smooth, undulated topography on which minima could also be reliably mapped by the STM tip. Herein, horizontal profiles (length: ±3 nm) were recorded that cut through the cluster maxima. Then, the cluster height was determined as the difference between the maximum and minimum in the height profile. 2) The h-BN/Rh(111) surface showed a flat topography with steep holes that had a flat bottom. This bottom could not be easily imaged by the STM tip and, if the film was not perfect (as in our study), it was measured with a depth that de-

pended on the diameter of the hole. Therefore, we determined the cluster height by referencing the cluster maxima to the overall mean height of the surface around the clusters. Such a reference is reliable because the background correction works perfectly over the whole imaged area (Figure 6). Owing to the much-stronger interactions of the clusters with this substrate and because the film was not perfectly uniform, the histogram did not show the well-separated peaks that were observed for g/Rh(111). However, the peak maxima in the height distribution can be assigned to layers, if we assign a height of one layer (which is consistent with the observation that OR occurs) to the smallest clusters that appear in the 700 K histogram. The thus-required upshift of 1.3 Å in the height values is larger than the depth of the h-BN holes (0.6 Å), which was calculated by using ab initio DFT[35] and might be related to electronic effects.

Theory

Calculations were performed by using the VASP-DFT package, with a plane-wave basis (kinetic energy cutoff: 400 eV), PAW pseudopotentials,[36] and the PW91 generalized gradient approximation (GGA) for the exchange-correlation potential.[37] Because the unit cell that was employed herein was rather large, we used in most of our calculations a single k-point (the Γ point) for sampling of the surface Brillouin zone (SBZ) in previous calculations of graphene that was adsorbed onto Ru(0001), by employing the same unit cell (but with the lattice parameter of Ru), we checked that the results remained essentially the same by employing (3×3×1) sampling of the SBZ.[18b] For the optimization of the various structures, convergence was achieved for forces smaller than 0.001 eV Å^{-1}. The Rh(111) surface consisted of three layers, with the optimized Rh lattice parameter $a = 2.707$ Å, in agreement with the experimental value ($a = 2.689$ Å); in the structural relaxations, the bottom layer of the substrate slab was fixed. In simulations of the adsorption of Pd$_{19}$ clusters, the supercell had an (11×11) lateral periodicity of the three-layer Rh(111) slab, a (12×12) layer of graphene, and a vacuum region, which was large enough to ensure no interaction between periodic replicas; the vacuum region for the bare Rh(111) system was taken as 20.7 Å, for the bare g/Rh(111) system as 19.7 Å, and for a two-layer Pd$_{19}$ cluster adsorbed at the r-hcp site as 16.3 Å. The relaxed configuration of the (11×11) structure exhibited a strong vertical modulation of the epitaxial graphene layer, with the highest C atom lying 3.88 Å above the underlying Ru topmost layer and the lowest-lying C atom at a distance of 2.06 Å, thereby resulting in a height modulation of 1.81 Å.

Acknowledgements

[1] C. H. Bartholomew, *Appl. Catal. A* **2001**, *212*, 17–60.
[2] J. R. Rostrup-Nielsen, *Catal. Today* **1993**, *18*, 125–145.
[3] a) H. L. Xin, J. A. Mundy, Z. Y. Liu, R. Cabezas, R. Hovden, L. F. Kourkoutis, J. L. Zhang, N. P. Subramanian, R. Makharia, F. T. Wagner, D. A. Muller, *Nano Lett.* **2012**, *12*, 490–497; b) M. A. Newton, C. Belver-Coldeira, A. Martinez-Arias, M. Fernandez-Garcia, *Nat. Mater.* **2007**, *6*, 528–532.
[4] D. W. Goodman, *Surf. Rev. Lett.* **1995**, *2*, 9–24.
[5] W. Ostwald, *Z. Phys. Chem.* **1900**, *34*, 495–503.
[6] M. v. Smoluchowski, *Phys. Z.* **1916**, *17*, 557–571; M. v. Smoluchowski, *Phys. Z.* **1916**, *17*, 585–599.
[7] a) M. J. J. Jak, C. Konstapel, A. van Kreuningen, J. Verhoeven, J. W. M. Frenken, *Surf. Sci.* **2000**, *457*, 295–310; b) A. Howard, C. E. J. Mitchell, R. G. Egdell, *Surf. Sci.* **2002**, *515*, L504–L508; c) T. W. Hansen, PhD Thesis, Technical University of Denmark, **2006**.
[8] a) I. M. Lifshitz, V. V. Slyozov, *Phys. Chem. Solids* **1961**, *19*, 35–50; b) C. Wagner, *Z. Elektrochem.* **1961**, *65*, 581–591; c) M. Kahlweit, *Adv. Colloid Interface Sci.* **1975**, *5*, 1–35.
[9] B. K. Chakraverty, *J. Phys. Chem. Solids* **1967**, *28*, 2401–2412.
[10] R. Finsy, *Langmuir* **2004**, *20*, 2975–2976.
[11] a) C. G. Granqvist, R. A. Buhrman, *Appl. Phys. Lett.* **1975**, *27*, 693–694; b) C. G. Granqvist, R. A. Buhrman, *J. Catal.* **1976**, *42*, 477–479.
[12] P. Wynblatt, N. A. Gjostein, *Prog. Solid State Chem.* **1975**, *9*, 21–58.
[13] A. K. Datye, Q. Xu, K. C. Kharas, J. M. McCarty, *Catal. Today* **2006**, *111*, 59–67.
[14] S. B. Simonsen, I. Chorkendorff, S. Dahl, M. Skoglundh, J. Sehested, S. Helveg, *J. Am. Chem. Soc.* **2010**, *132*, 7968–7975.
[15] K. Morgenstern, G. Rosenfeld, G. Comsa, *Surf. Sci.* **1999**, *441*, 289–300.
[16] a) S. E. Wanke, *J. Catal.* **1977**, *46*, 234–237; b) C. G. Granqvist, R. A. Buhrman, *J. Catal.* **1977**, *46*, 238–242.
[17] R. Popescu, R. Schneider, D. Gerthsen, A. Böttcher, D. Löffler, P. Weis, M. M. Kappes, *Surf. Sci.* **2009**, *603*, 3119–3125.
[18] a) B. Wang, M. L. Bocquet, *J. Phys. Chem. Lett.* **2011**, *2*, 2341–2345; b) B. Wang, B. Yoon, M. König, Y. Fukamori, F. Esch, U. Heiz, U. Landman, *Nano Lett.* **2012**, *12*, 5907–5912.
[19] G. Rosenfeld, K. Morgenstern, M. Esser, G. Comsa, *Appl. Phys. A* **1999**, *69*, 489–496.
[20] a) G. Rosenfeld, A. F. Becker, B. Poelsema, L. K. Verheij, G. Comsa, *Phys. Rev. Lett.* **1992**, *69*, 917–920; b) C. Massobrio, P. Blandin, *Phys. Rev. B* **1993**, *47*, 13687–13695.
[21] T. Michely, M. Hohage, M. Bott, G. Comsa, *Phys. Rev. Lett.* **1993**, *70*, 3943–3946.
[22] B. Wang, M. Caffio, C. Bromley, H. Fruchtl, R. Schaub, *ACS Nano* **2010**, *4*, 5773–5782.
[23] J. Knudsen, P. J. Feibelman, T. Gerber, E. Granas, K. Schulte, P. Stratmann, J. N. Andersen, T. Michely, *Phys. Rev. B* **2012**, *85*, 035407.
[24] J. A. Moulijn, A. E. van Diepen, F. Kapteijn, *Appl. Catal. A* **2001**, *212*, 3–16.
[25] a) O. Bunk, M. Corso, D. Martoccia, R. Herger, P. R. Willmott, B. D. Patterson, J. Osterwalder, I. van der Veen, T. Greber, *Surf. Sci.* **2007**, *601*, L7L10; b) S. Berner, M. Corso, R. Widmer, O. Groening, R. Laskowski, P. Blaha, K. Schwarz, A. Goriachko, H. Over, S. Gsell, M. Schreck, H. Sachdev, T. Greber, J. Osterwalder, *Angew. Chem.* **2007**, *119*, 5207–5211; *Angew. Chem. Int. Ed.* **2007**, *46*, 5115–5119.
[26] a) H. Dil, J. Lobo-Checa, R. Laskowski, P. Blaha, S. Berner, J. Osterwalder, T. Greber, *Science* **2008**, *319*, 1824–1826; b) A. Goriachko, Y. B. He, H. Over, *J. Phys. Chem. C* **2008**, *112*, 8147–8152.
[27] D. E. Sanders, A. E. Depristo, *Surf. Sci.* **1992**, *264*, L169–L176.
[28] T. Gerber, J. Knudsen, P. J. Feibelman, E. Granas, P. Stratmann, K. Schulte, J. N. Andersen, T. Michely, *ACS Nano* **2013**, *7*, 2020–2031.
[29] a) S. Kunz, F. F. Schweinberger, V. Habibpour, M. Rottgen, C. Harding, M. Arenz, U. Heiz, *J. Phys. Chem. C* **2010**, *114*, 1651–1654; b) T. Engel, G. Ertl, *J. Chem. Phys.* **1978**, *69*, 1267–1281.

[30] M. Di Vece, D. Grandjean, M. J. Van Bael, C. P. Romero, X. Wang, S. Decoster, A. Vantomme, P. Lievens, *Phys. Rev. Lett.* **2008**, *100*, 236105.

[31] N. V. Piskunov, Y. T. Sinyapkin, V. M. Kulgavchuk, N. A. Protopopov, *J. Eng. Phys. Thermophys.* **2001**, *74*, 1217–1220.

[32] a) A. Sanchez, S. Abbet, U. Heiz, W. D. Schneider, H. Hakkinen, R. N. Barnett, U. Landman, *J. Phys. Chem. A* **1999**, *103*, 9573–9578; b) U. Landman, B. Yoon, C. Zhang, U. Heiz, M. Arenz, *Top. Catal.* **2007**, *44*, 145–158.

[33] U. Heiz, F. Vanolli, L. Trento, W. D. Schneider, *Rev. Sci. Instrum.* **1997**, *68*, 1986–1994.

[34] M. Sicot, S. Bouvron, O. Zander, U. Rudiger, Y. S. Dedkov, M. Fonin, *Appl. Phys. Lett.* **2010**, *96*, 093115.

[35] R. Laskowski, P. Blaha, T. Gallauner, K. Schwarz, *Phys. Rev. Lett.* **2007**, *98*, 106802.

[36] G. Kresse, D. Joubert, *Phys. Rev. B* **1999**, *59*, 1758–1775.

[37] a) J. P. Perdew in *Electronic Structure of Solids* (Eds.: P. Ziesche, H. Eschring), Akademie, Berlin, **1991**; b) J. P. Perdew, J. A. Chevary, S. H. Vosko, K. A. Jackson, M. R. Pederson, D. J. Singh, C. Fiolhais, *Phys. Rev. B* **1992**, *46*, 6671–6687; c) J. P. Perdew, J. A. Chevary, S. H. Vosko, K. A. Jackson, M. R. Pederson, D. J. Singh, C. Fiolhais, *Phys. Rev. B* **1993**, *48*, 4978–4978.